

Finite element modeling of spontaneous emission of a quantum emitter at nanoscale proximity to plasmonic waveguides

Yuntian Chen, Torben Roland Nielsen, Niels Gregersen, Peter Lodahl, and Jesper Mørk
*DTU Fotonik, Department of Photonics Engineering,
Ørstedss Plads, Building 345v, DK- 2800 Kgs. Lyngby, Denmark.*
(Dated: May 21, 2018)

We develop a self-consistent finite element method to study spontaneous emission at nanoscale proximity of plasmonic waveguides. In the model, it is assumed that only one guided mode is dominantly excited by the quantum emitter. With such one dominating mode assumption, the cross section of the plasmonic waveguide can be arbitrary. We apply our numerical method to calculate the coupling of a quantum emitter to a cylindrical nanowire and a rectangular waveguide, and compare the cylindrical nanowire to previous work valid in quasistatic approximation. The fraction of the energy coupled to the plasmonic mode can be calculated exactly, which can be used to determine the single optical plasmon generation efficiency for a quantum emitter. For a gold nanowire we observe agreement with the quasistatic approximation for radii below 20 nm, but for larger radii the total decay rate is up to 10 times larger. For the rectangular waveguide we estimate an optimized value for the spontaneous emission factor β of up to 80%.

PACS numbers: 42.50.Pq, 73.20.Mf, 78.55.-m

I. INTRODUCTION

It has long been realized that the spontaneous emission rate is not an intrinsic property of a quantum emitter itself¹. The general explanation is that the spontaneous emission rate depends on the transition strength between the upper and lower level of the quantum emitter and the local density of optical states. The local density of states measures the available number of electromagnetic modes into which the photons can be emitted at a specific location of the emitter, and can be manipulated by tailoring the photonic environment of the emitter. A number of structures such as interfaces^{2,3}, cavities^{4,5}, photonic crystals^{6,7} and waveguides^{8,9} have already been used to modify the spontaneous emission rate. Apart from fundamental studies, engineering the spontaneous emission rate of a quantum emitter can lead to new possibilities to boost the efficiency of optoelectronic devices, i.e., single-photon sources, low threshold lasers, and LED-lightening.

As an alternative to dielectric materials, the spontaneous emission rate can be manipulated by subwavelength metallic systems, which support surface plasmon polaritons. Surface plasmon polaritons are electromagnetic excitations associated with charge density waves on the surface of a conducting object. The tight confinement of the electromagnetic field to the metal-dielectric interface due to the boundary condition constraints gives the possibility of inventing new ways to enhance light-matter interaction, such as efficient single optical plasmon generation^{10,11}, single molecule detection with surface-enhanced Raman scattering^{12,13}, enhanced photoluminescence from quantum wells¹⁴, and nanoantenna modified spontaneous emission^{15,16,17}.

Although limited by the intrinsic losses of the metals in the optical frequency range, different metallic structures have been extensively studied in the last few years due to the possibilities of integration and miniaturization. The dramatic enhancement of the field intensity due to the field concentration and geometric slowing down of the mode propagation provides an excellent platform to study single photon nonlinear optics¹⁸, and light matter interaction at the single-emitter-single-photon level. There are also considerable interests in surface plasmons for in sub-wavelength optics¹⁹ and applications in sensing, near field imaging, waveguiding and switching below the diffraction limit^{20,21,22,23}. The study of plasmonic effects to enhance light-matter interaction and the preferential emission of, e.g., a quantum dot into a desired mode is currently a hot research topic. It is important for solid-state quantum information devices as well as for improving our understanding of light-matter interaction at the nanoscale. So far, there are a few theoretical papers^{11,24} on this topic, and they employ simplifying assumptions that limit their applicability for analysing realistic structures, e.g. by assuming geometrical shapes that are inconsistent with current fabrication technology and making assumptions that are only valid at some length scales. The realistic description of all competing, radiative and non-radiative, decay channels for an emitter placed in close proximity to a plasmonic waveguide is important in order to understand the physics and the fundamental limitations.

The present paper focuses on modeling of the spontaneous emission of a quantum emitter at nanoscale proximity to the realistic plasmonic waveguides by using a finite element method, with special emphasis on calculating the spontaneous emission β factor. The β factor describes the fraction of the emitted energy that is coupled to the plasmonic mode. Subwavelength waveguiding of plasmons in metallic structures has been studied theoretically^{22,25} and has also been observed in a number of recent experiments²³. Enhanced spontaneous emission of an emitter coupled

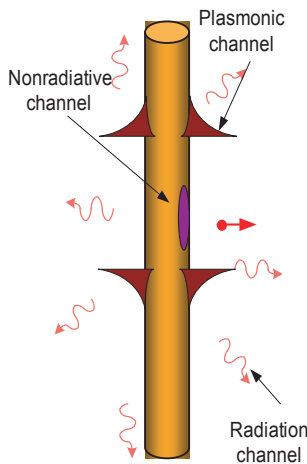


FIG. 1: Different emission channels involved in the decay process of a quantum emitter (red dot) coupled to a plasmonic waveguide. In the radiation channel the photons are traveling in free space. In the plasmonic channel the plasmonic modes are excited and guided by the metallic nanowire. In the non-radiative channel, electron hole pairs are generated.

to plasmonic waveguides has been proposed^{11,26} and experimentally demonstrated¹⁰ recently. Chang et al.²⁴ studied the spontaneous emission of an emitter coupled to a metallic nanowire by using the quasistatic approximation. Jun et al.²⁶ employed a FDTD numerical method to study the different spontaneous emission decay rates of an emitter coupled to a metallic slot waveguide, but with assumptions for the local density of states of the plasmonic mode. A self-consistent model with rigorous treatment of all the spontaneous decay rates involved, i.e. radiative as well as non-radiative, has not been presented in the literature. The aim of this paper is to provide such a detailed modeling.

As shown in Fig. 1, we consider an ideal quantum emitter coupled to a plasmonic waveguide. The excitation energy of the quantum emitter can be dissipated either radiatively or non-radiatively. Radiative relaxation is associated with the emission of a photon, whereas non-radiative relaxation can be various pathways such as coupling to vibrations, resistive heating of the environment, or quenching by other quantum emitters. The resistive heating of the metallic waveguide is then the only mechanism of non-radiative relaxation considered in our model. The quantum emitter is positioned in the vicinity of the metallic nanowire, thus there are three channels for the quantum emitter to decay into, i.e., the radiative channel, the plasmonic channel and the non-radiative channel. The corresponding decay rates are denoted by γ_{rad} , γ_{pl} , and γ_{nonrad} , respectively. The radiative channel is the spontaneous emission in the form of far field radiation. The plasmonic channel is the excitation of the plasmonic mode, which is guided by the plasmonic waveguide. The non-radiative channel is associated with the resistive heating of the lossy metals, which is due to electron-hole generation inside the metals. The spontaneous emission β factor is defined by $\beta = \frac{\gamma_{pl}}{\gamma_{total}}$, where γ_{total} is the sum of the three rates, $\gamma_{total} = \gamma_{rad} + \gamma_{nonrad} + \gamma_{pl}$. The β factor gives the probability of the photon “coupling” to the plasmonic mode, when the single quantum emitter decays.

This paper is organized as follows. In Sec. II, the computational principle and the numerical method are presented, First we study the dispersion relation and the mode properties of the plasmonic waveguide, and then we calculate the decay rate into the plasmonic channel in a 2D model by taking advantage of the translation symmetry of the waveguides. Finally, the wave equation with a current source in a 3D model is solved numerically, and the total decay rate of the quantum emitter is extracted by calculating the normalized total power emission of the current source. Section III presents the results and discussion obtained by applying the numerical method to two different plasmonic waveguides. Section IV concludes the paper.

II. COMPUTATIONAL APPROACH

A. Dispersion relation and decay rate into the plasmonic channel

The starting point of the numerical analysis of the waveguide is the wave equation for the electric field,

$$\nabla \times \left(\frac{\nabla \times \bar{E}}{\mu_r} \right) - k_0^2 \epsilon_r \bar{E} = 0,$$

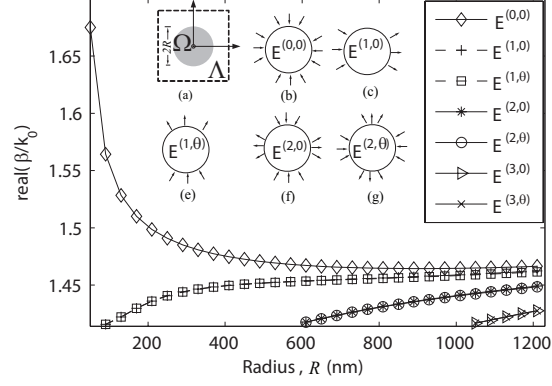


FIG. 2: Dispersion relation versus radius for the metallic nanowire . Inset (a) shows the waveguide structure. Inset (b-g) show field orientation of the possible eigenmodes supported by the waveguide.

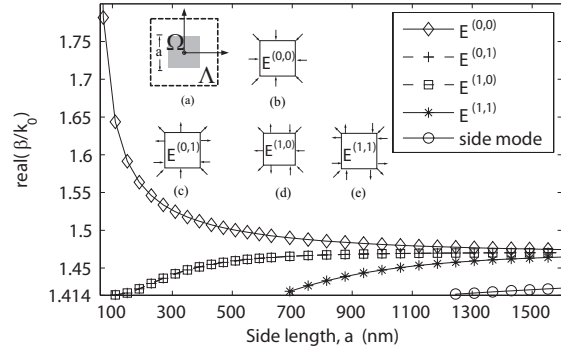


FIG. 3: Dispersion relation versus side length of the square plasmonic waveguides . Inset (a) shows the waveguide structure. Inset (b-e) shows field orientation of the possible eigenmodes supported by square plasmonic waveguides.

where $k_0 = \omega\sqrt{\varepsilon_0\mu_0}$ is the vacuum wave number, ε_r denotes the relative dielectric constant and μ_r represents the relative permeability constant, which is a constant in our model. Due to the invariance along the Z axis, the Z-dependence of the solution to the wave equation must be that of a plane wave (complex exponential),

$$\vec{E}(x, y, z) = \vec{E}_\alpha(x, y)e^{j(\omega t - \beta z)}.$$

Through out the paper, j denotes $\sqrt{-1}$. For the guided plasmonic modes, at a specific frequency ω two quantization indices are needed to specify a complete set of orthogonal modes, i.e., $\alpha = \{p, \beta\}$. β denotes the propagation constant (the component of the wave vector along the Z-axis), and the index p represents the polarization of the mode. The waveguide structure examined consists of two regions Ω and Λ . Ω is the lossy metal core, which is surrounded by an infinite lossless dielectric medium Λ . The transverse component of the wave vector fulfills $(jk_{i\perp})^2 + \beta^2 = \frac{\omega^2}{c^2}\varepsilon_i$ with $i \in [\Omega, \Lambda]$, where $k_{i\perp}$ and ε_i are the transverse component of the wave vector and the relative permittivity.

The finite element method can be utilized as a numerical tool to calculate the guided plasmonic modes. The infinite dielectric medium is truncated to perform the finite element analysis of the waveguide structure by placing the structure inside a computational window, which is large enough to guarantee the field vanishing at the boundary. Here, we consider an optical wavelength of $1 \mu\text{m}$ and the optical permittivities of the waveguide are $\varepsilon_\Omega = -50 - 3.85i$ and $\varepsilon_\Lambda = 2$, corresponding to gold and polymer²⁷. The dispersion and the field orientation of the possible modes for cylindrical and square waveguides are presented in Fig. 2 and Fig. 3 respectively. As shown in the inset of Fig. 2, these modes can be presented by two indices, where the first index denotes the number of the angular moment, m , and the second index describes the polarization degenerate mode with the same m . For example, if the $E^{m,0}$ denotes the mode with angular moment of m , then $E^{m,\theta}$ denotes the corresponding degenerated mode, the field distribution of which is rotated by θ along the z axis compared with $E^{m,0}$, where $\theta = 2\pi/2m$. As pointed out by Takahara et al.²², the fundamental mode $E^{(0,0)}$ does not have a cutoff size of the radius, which is confirmed from the dispersion relation in Fig. 2. The modes supported by the metallic nanowire preserve the cylindrical symmetry of the waveguide.

Due to the constraints from the boundary conditions, only TM modes exist. For the square surface plasmon-polariton waveguides, the fundamental modes, which were studied by Jung et al.²⁸, can be labeled in terms of two indices, which denote the number of sign changes in the dominant component of the electric field along the x and y axes respectively. Both plasmonic waveguides support one fundamental mode ($E^{0,0}$) without any cutoff size of the metal core, and the corresponding propagation constants increase when the size of the metal core is further shrunk, which slows down the propagating plasmonic mode. Such geometric slowing down enhances the local density of the states and the coupling efficiency to the nearby quantum emitter. In the following calculations, the size of metal core is restricted below the cutoff size of higher order modes so that only a single mode is supported.

The electric-field dyadic Green's function for a specific guided plasmonic mode is constructed from the numerical calculation of the electric field. In the following part we will explain how to construct the electric-field dyadic Green's function for one guided plasmonic mode²⁹.

The electric dyadic Green function $\bar{\bar{G}}(\bar{r}, \omega)$ is defined by

$$[\nabla \times \nabla \times -k_0^2 \varepsilon(\bar{r})] \bar{\bar{G}}(\bar{r}, \omega) = \bar{\bar{I}} \delta(\bar{r} - \bar{r}'),$$

where $\bar{\bar{I}}$ is the unit dyad. Rigorously speaking, the operator defined by $L = [\nabla \times \nabla \times -k_0^2 \varepsilon(\bar{r})]$ does not have a set of complete and orthogonal eigenmodes due to its non Hermitian character. Without loss of generality, we adopt biorthogonality in the present paper to form a complete set of "orthogonal" modes of the waveguides initially, and then we will end up with an approximation from the power orthogonality for our plasmonic waveguides. Suppose that \bar{E}_n are a set of eigensolutions defined by \hat{L} , the biorthogonal modes \bar{E}_n^\dagger are defined as the eigensolutions of the adjoint operator denoted by \hat{L}^\dagger , which is obtained from the operator \hat{L} by replacing $\varepsilon(\bar{r})$ with its complex conjugate. The biorthogonality condition is given by

$$\int \varepsilon(\bar{r}) \bar{E}_n(\bar{r}) [\bar{E}_m^\dagger(\bar{r})]^* d^3 r = \delta_{nm} N_n, \quad (1)$$

with the completeness relation $\sum_n \frac{\varepsilon(\bar{r}) \bar{E}_n(\bar{r}) [\bar{E}_n^\dagger(\bar{r}')]^*}{N_n \lambda_n} = \bar{\bar{I}} \delta(\bar{r} - \bar{r}')$. From the biorthogonal completeness relation, the dyadic Green function $\bar{\bar{G}}(\bar{r}, \omega)$ can be constructed from the eigenfunction expansion as follows²⁹,

$$\begin{aligned} \bar{\bar{G}}(\bar{r}, \bar{r}') &= \bar{\bar{G}}_{GT}(\bar{r}, \bar{r}') + \bar{\bar{G}}_{GL}(\bar{r}, \bar{r}') \\ &= \sum_n \frac{\bar{E}_n(\bar{r}) \cdot [\bar{E}_n^\dagger(\bar{r}')]^*}{N_n \lambda_n} + \sum_n \frac{\nabla \phi_n(\bar{r}) \cdot [\nabla \phi_n^\dagger(\bar{r}')]^*}{M_n k_0^2} \end{aligned} \quad (2)$$

where the generalized transverse part of the dyadic Green's function, $\bar{\bar{G}}_{GT}$, is constructed from the complete set of transverse eigenfunction $\bar{E}_n(\bar{r})$ given by,

$$\begin{aligned} -\nabla \times \nabla \times \bar{E}_n(\bar{r}) + k_0^2 \varepsilon(\bar{r}) \bar{E}_n(\bar{r}) &= \lambda_n \varepsilon(\bar{r}) \bar{E}_n(\bar{r}), \\ \nabla \cdot [\varepsilon(\bar{r}) \bar{E}_n(\bar{r})] &= 0, \end{aligned} \quad (3)$$

with the eigenvalue λ_n . The longitudinal or quasistatic part $\bar{\bar{G}}_{GL}$ is constructed from longitudinal eigenfunction that can be found from a complete set of scalar eigenmodes $\phi_n(\bar{r})$ satisfying

$$\nabla \cdot [\varepsilon(\bar{r}) \nabla \phi_n(\bar{r})] = \sigma_n \phi_n(\bar{r}) \quad (4)$$

with the biorthogonality relation, $\int \varepsilon(\bar{r}) \nabla \phi_n(\bar{r}) \cdot [\nabla \phi_n^\dagger(\bar{r}')]^* d^3 r = \delta_{nm} M_n$. Since we are studying the guided plasmonic mode, which describes the field solution in the absence of electric charge ($\nabla \cdot [\varepsilon(\bar{r}) \bar{E}_n(\bar{r})] = 0$), the longitudinal component will vanish in the following calculations.

By applying the principle of constructing the electric-field dyadic Green's function to the case of a plasmonic waveguide, we find the contribution to the dyadic Green's function from the plasmonic modes as

$$\bar{\bar{G}}_{pl}(\bar{r}, \bar{r}') = \sum_p \int_{-\infty}^{+\infty} \frac{\varepsilon_\Lambda \bar{E}_\alpha(\bar{r}) \cdot [\bar{E}_{\tilde{\alpha}}^\dagger(\bar{r}')]^* e^{-j\beta(z-z')}}{[k_0^2 \varepsilon_\Lambda - (\beta^2 - k_{\Lambda\perp}^2)] N} d\beta \quad (5)$$

where $\tilde{\alpha} = \{p, -\beta\}$, and the normalization factor N is given by $\delta(\beta - \beta') \delta_{pp'} N = \int \varepsilon(\bar{r}) \bar{E}_\alpha(\bar{r}) [\bar{E}_{\tilde{\alpha}}^\dagger(\bar{r})]^* d^3 r = 2\pi \delta(\beta - \beta') \delta_{pp'} \int \varepsilon(\bar{r}) \bar{E}_\alpha(\bar{r}) [\bar{E}_{\tilde{\alpha}}^\dagger(\bar{r})]^* dx dy$, which can be further simplified as $N = 2\pi \int \varepsilon(\bar{r}) \bar{E}_\alpha(\bar{r}) [\bar{E}_{\tilde{\alpha}}^\dagger(\bar{r})]^* dx dy$, where

α' denotes $\{p', -\beta'\}$. For one plasmonic mode, the expression (5) is evaluated in closed form by the method of contour integration as the integrand decays to zero at infinity in the upper and the lower β plane,

$$\begin{aligned}\bar{G}_{pl}(\bar{r}, \bar{r}) &= j2\pi \frac{\varepsilon_2 \bar{E}_{\alpha_0}(\bar{r}) \cdot [\bar{E}_{\alpha_0}^\dagger(\bar{r})]^*}{\frac{d(k_0^2 \varepsilon_2)}{d\beta} N} \\ &= \frac{j\pi c^2 \bar{E}_{\alpha_0}(\bar{r}) \cdot [\bar{E}_{\alpha_0}^\dagger(\bar{r})]^*}{\omega N v_g},\end{aligned}\quad (6)$$

where v_g is the group velocity, defined by $v_g = d\omega/d\beta$. The corresponding density of states for one plasmonic mode can be calculated from the dyadic Green function according to Novotny³⁰, $\rho_\mu(r_0, \omega_0) = 6\omega[\bar{n}_\mu \cdot \text{Im}\{\bar{G}(r_0, r_0, \omega_0)\} \cdot \bar{n}_\mu]/(\pi c^2)$, where n_μ is the unit vector of the dipole moment. If the dipole emitter is oriented along the X axis, the density of states for the plasmonic mode is given by $\rho_{pl}(\bar{r}, \omega) = 6|E_{\alpha,x}(\bar{r})|^2/(Nv_g)$. The spontaneous emission decay rate into the plasmonic mode can be calculated by $\gamma_{pl} = \frac{\pi\omega_0}{3\hbar\varepsilon_0} |\mu|^2 \rho_{pl}(\bar{r}, \omega)$. Normalized by the spontaneous emission decay rate in the vacuum, the emission enhancement due to the plasmonic excitation is

$$\frac{\gamma_{spp}}{\gamma_0} = \frac{6\pi^2 c^3 E_{\alpha_0,X}(\bar{r}) [E_{\alpha_0,X}^\dagger(\bar{r})]^*}{\omega_0^2 N v_g}. \quad (7)$$

Eq. (7) gives a general expression of the spontaneous emission decay rate into a guided mode, supported by a lossy or lossless waveguide. In dielectric waveguides, losses are generally small, and the biorthogonal modes \bar{E}_m^\dagger can approximately be replaced by the orthogonal mode \bar{E}_m . Such an approximation is also valid for our plasmonic waveguide, where the imaginary part of the propagation constant for the fundamental mode is around 1% of the real part. According to Snyder³¹, the group velocity can be calculated by $v_g = \int_{A_\infty} (\bar{E} \times \bar{H}^*) \cdot \bar{z} dA / \int_{A_\infty} \varepsilon_0 \varepsilon(r) |\bar{E}(r)|^2 dA$, where A_∞ denotes integration over the transverse plane. By applying the power orthogonal approximation and the explicit form of the group velocity to Eq. (7), we can reach the following expression for the plasmonic decay rate of the fundamental mode,

$$\frac{\gamma_{pl}}{\gamma_0} = \frac{3\pi c \varepsilon_0 E_{\alpha_0,X}(\bar{r}) E_{\alpha_0,X}^*(\bar{r})}{k_0^2 \int_{A_\infty} (\bar{E} \times \bar{H}^*) \cdot \bar{z} dA}. \quad (8)$$

B. Total decay rate

As described in the previous subsection, the well defined field components in the transverse plane of the waveguide give the possibility of constructing the dyadic Green's function numerically. The reason is that the field is concentrated around the metallic core and is decaying to zero on the borders when the modeling domain is reasonably large. Hence, the perfect electric conductor boundary condition is implemented to truncate the 2D modeling domain. However, for the radiation modes, the field components in the transverse plane of the waveguide do not vanish no matter how large the modeling domain is. Hence, it is extremely difficult to construct the dyadic Green's function numerically for the radiation modes in a similar way as for the guided mode. Therefore, we implement a 3D model to include the radiation modes, as well as the nonradiative contributions, by solving the wave equation with a harmonic (time dependent) source term,

$$[\nabla \times \frac{1}{\mu_r} \nabla \times - k_0^2 \varepsilon(\bar{r})] \bar{E}(\bar{r}, \omega) + j\omega \mu_0 \bar{J}(\omega) = 0. \quad (9)$$

If we introduce a test function $\bar{F}(\bar{r}, \omega)$, we can construct the functional corresponding to the wave equation in the following way³²,

$$\begin{aligned}L &= \iiint_V [\nabla \times \frac{1}{\mu_r} \nabla \times - k_0^2 \varepsilon(\bar{r})] \bar{E}(\bar{r}, \omega) \cdot \bar{F}^*(\bar{r}, \omega) dV + \iiint_V j\omega \mu_0 \bar{J}(\omega) \cdot \bar{F}^*(\bar{r}, \omega) dV \\ &= \iiint_V \frac{1}{\mu_r} \nabla \times \bar{E}(\bar{r}, \omega) \cdot \nabla \times \bar{F}^*(\bar{r}, \omega) dV - \iiint_V k_0^2 \varepsilon(\bar{r}) \bar{E}(\bar{r}, \omega) \cdot \bar{F}^*(\bar{r}, \omega) dV + \iiint_V j\omega \mu_0 \bar{J}(\omega) \cdot \bar{F}^*(\bar{r}, \omega) dV \\ &+ \oint_{\partial V} \bar{F}^*(\bar{r}, \omega) \cdot [\frac{1}{\mu_r} \bar{n} \times \nabla \times \bar{E}(\bar{r}, \omega)] ds,\end{aligned}\quad (10)$$

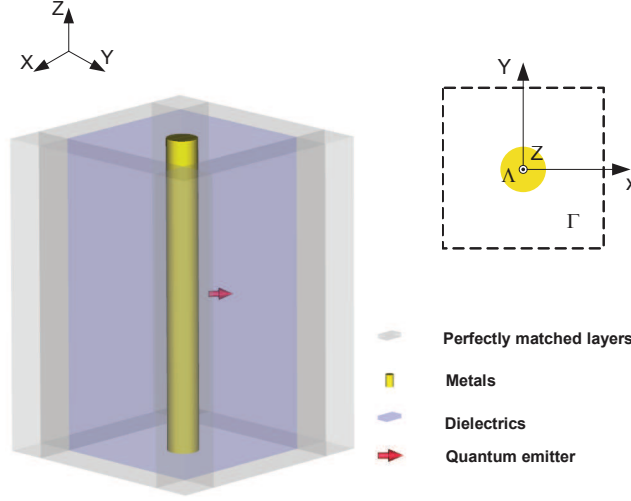


FIG. 4: A single quantum emitter coupled to a metallic nanowire. The grey transparent region represents the perfectly matched layers, the mode matching boundary condition is applied on the top and the bottom of the structure. The quantum emitter is implemented by an electric line current.

where ∂V denotes the surface that encloses the volume V , and \bar{n} denotes the outward unit normal vector to the surface of the modeling domain. This is the variational formulation of the wave equation, which is required to hold for all the test functions. Eq. (10) enables us to formulate the finite element solution for such a boundary-value problem by employing the standard finite element solution procedures, including discretization and factorization of a sparse matrix³². The boundary-value problem defined by Eq. (10) was solved by utilizing a commercial software package, COMSOL Multiphysics³⁷.

It is crucial to truncate the computational domain properly. As shown in Fig. 4, we have two strategies to truncate the modeling domain: I) In the X-Y plane, the computation domain is truncated by the perfectly matched layers with thickness of half a wavelength in vacuum. II) Along the Z-axis, the computation domain is terminated by mode matching boundary conditions, which will induce a certain amount of reflection from the radiation mode and the higher order plasmonic modes if they exist. Essentially, the mode matching boundary is an absorbing wall, which behaves as a sink of electromagnetic waves. There are different options of realizing the mode matching boundary to absorb a single mode, depending on whether the absorbed mode is TE, TM or a hybrid mode. For a pure TM or TE mode, it can be matched by simply applying the conditions,

$$\frac{1}{\mu_r} \bar{n} \times \nabla \times \bar{E}(\bar{r}, \omega) = \frac{k_0^2 \epsilon_r \bar{E}_t(\bar{r}, \omega)}{j\beta}, \quad TM; \quad (11a)$$

$$\frac{1}{\mu_r} \bar{n} \times \nabla \times \bar{E}(\bar{r}, \omega) = j\beta \bar{n} \times \frac{1}{\mu_r} \bar{n} \times \bar{E}_t(\bar{r}, \omega), \quad TE; \quad (11b)$$

on the boundary, where β is the propagation constant, and $\bar{E}_t(\bar{r}, \omega)$ is the tangential components of the dependent variable $\bar{E}(\bar{r}, \omega)$ on the boundaries in the numerical model. The mode matching boundary condition for the hybrid mode can be implemented as

$$\frac{1}{\mu_r} \bar{n} \times \nabla \times \bar{E}(\bar{r}, \omega) = -j\omega \mu_0 \bar{n} \times \bar{H}_0, \quad (12)$$

where $\bar{E}(\bar{r}, \omega)$ is the dependent variable solved in the 3D model, and \bar{H}_0 denotes the matched mode that is applied. In our model, \bar{H}_0 corresponds to the fundamental hybrid mode supported by the plasmonic waveguide. It is calculated from the 2D eigenvalue problem, and is given by

$$\bar{H}_0 = \sqrt{\frac{\gamma_{pl} P_0}{P_{2d}}} \bar{H}_{2d} e^{-j\beta L_0} = (H_{0x}, H_{0y}, H_{0z}). \quad (13)$$

Here, P_{2d} , \bar{H}_{2d} and β are the time averaged power flow, the magnetic field, and the propagation constant, respectively calculated from the 2D model, while P_0 denotes the normalization factor of the power emission in the 3D model, and L_0 represents the half length of the 3D model. Due to the losses of the metals, the magnitude of the magnetic

TABLE I: The relation of the 6 field components for the fundamental hybrid mode

Description	Relation
Tangential electric field, $s \in [x, y]$	$E_{2D,t}^s = \frac{\beta}{\omega\epsilon}(\bar{n} \times H_{2D,t})_s + \frac{j}{\omega\epsilon}(\nabla_t \times \bar{n} H_{2D}^n)_s$
Normal electric field	$E_{2D}^n = \frac{j}{\omega\epsilon}\bar{n} \cdot (\nabla_t \times H_{2D,t})$
Tangential magnetic field, $s \in [x, y]$	$H_{2D,t}^s = H_{2d,m}^s$
Normal magnetic field	$H_{2D}^n = jH_{2d,m}^z$

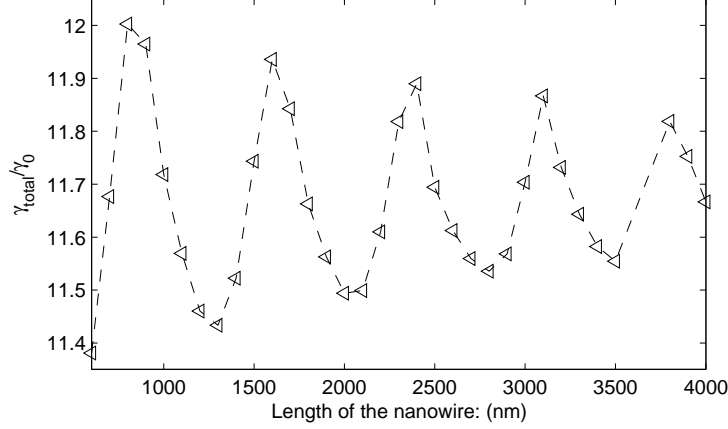


FIG. 5: Length dependence study of the total decay rate for the metallic nanowire. The radius of the metallic nanowire is 20 nm, the distance of emitter to the wire edge is 30nm.

field is a complex number. In order to guarantee that the phase of E_x at the position of the emitter is zero when the emitter is oriented horizontally, the extra phase $\phi = \arctan\left(\frac{\text{imag}(E_{2D}^x)}{\text{real}(E_{2D}^x)}\right)$ needs to be compensated, i.e., $\bar{H}_0 = \sqrt{\frac{\gamma_{pl}P_0}{P_{2d}}}\bar{H}_{2d}e^{-j(\beta L_0 + \phi)}$. In the 2D eigenvalue calculations, there are 6 components involved for the hybrid fundamental model, the relations of which are tabulated in Table I. The magnitudes of the magnetic field, $(H_{2d,m}^x, H_{2d,m}^y, H_{2d,m}^z)$, are the dependent variables, which are calculated directly from the 2D numerical model.

The total decay rate, γ_{total} , is extracted from the total power dissipation of the current source coupled to the nearby metallic waveguide, $\gamma_{total}/\gamma_0 = P_{total}/P_0$, where $P_{total} = 1/2 \int_V \text{Re}(J^* \cdot E_{total})dV$ is the power dissipation of the current source coupled to the metallic waveguide, and $P_0 = 1/2 \int_V \text{Re}(J^* \cdot E_0)dV$ is the emitted power by the same current source in vacuum. P_0 is a normalization factor, which is also used to normalize the power flow on the boundaries in Eq. (13). As demonstrated in Fig. 4, the field is generated by the current source, namely, the dipole emitter, which is implemented by a small electric line current. In our model, the dipole is oriented horizontally. For an electric current source with finite size of l ($l \ll \lambda_0$), and linear distribution of current I_0 , the dipole moment of the source³³ is, $\mu = jI_0l/\omega$. In order to avoid higher order multipole moments, the size of the current source should be restricted below a certain value. Our numerical test shows that the variation of the total power dissipation from the size dependence of the emitter is negligible when the size of emitter is shorter than 2 nm.

In order to check the validity of the mode matching boundary condition we studied the length dependence of the total decay rate for two different plasmonic waveguides. The length dependence of the total decay rate γ_{total} for the metallic nanowire is shown in Fig. 5. The fundamental mode supported by the metallic nanowire is TM, hence the mode matching boundary condition defined by Eq. (11a) is implemented. As can be seen from Fig. 5, the variations in the total decay rate are reduced by increasing L_0 , and the damped oscillation of the total decay rate with L_0 indicates a certain amount of reflection from radiation modes, which is confirmed by the period of the oscillation (equal to the wavelength in the media with $\epsilon = 2$). We also see that the variation of the total decay rate due to the length dependence is below $\pm 2.5\%$ due to the dominating excitation of the plasmonic mode when L_0 is larger than 1 μm . Basically, the accuracy of γ_{total}/γ_0 relies on the length of the plasmonic waveguide, accordingly we estimate the relative error on the computed data is $\pm 2.5\%$ in the following calculations for the metallic nanowire.

Regarding the square plasmonic waveguide, the condition defined by Eq. (13) is applied on the boundary to absorb the hybrid mode supported by the waveguide, where \bar{H}_0 is the magnetic field for the matched field. As shown in Fig. 6,

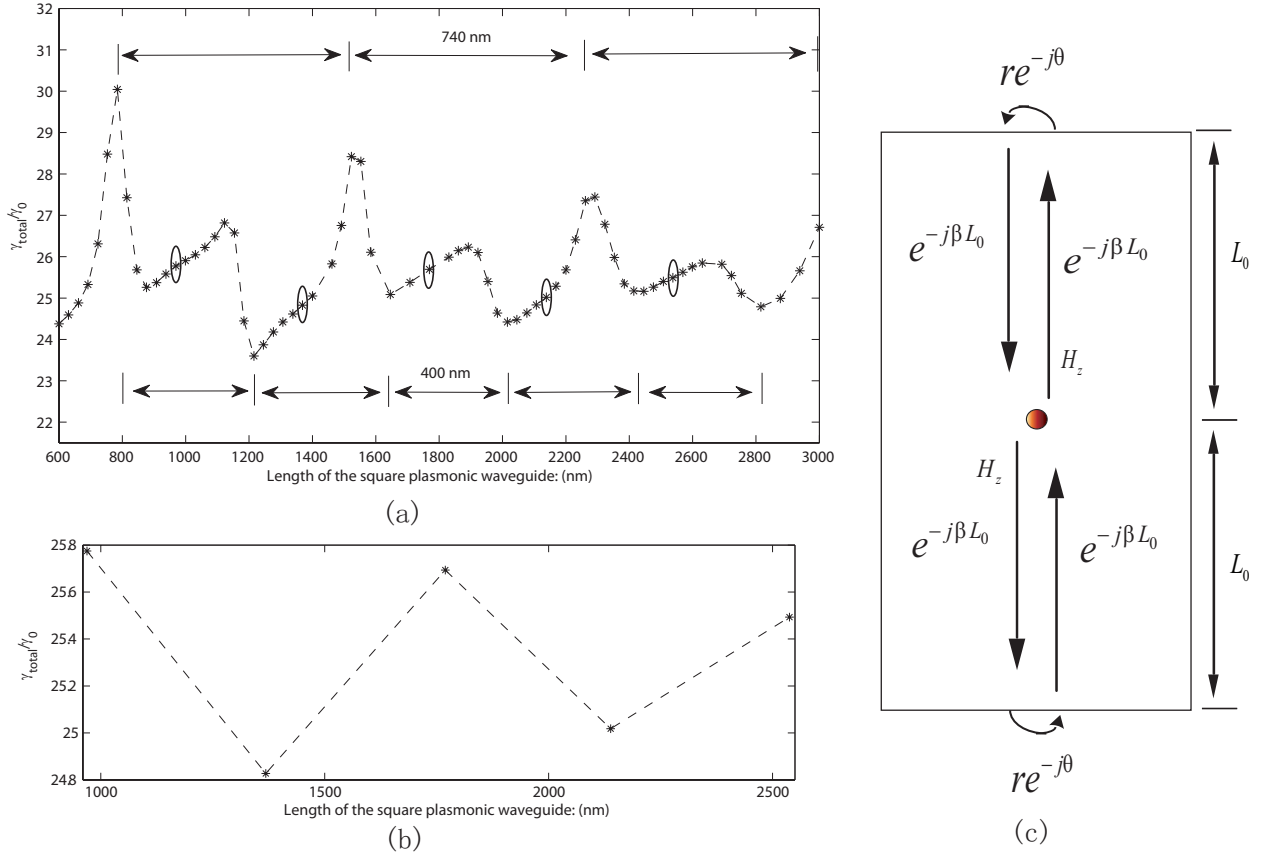


FIG. 6: (a) Length dependence of the total decay rate for the square plasmonic waveguide. The side length is 30nm, the distance of the emitter to the edge of the square metal core is 20 nm. (a) Length dependence study with damped oscillations. (b) Length dependence for the points from (a) (marked ellipses) where where $real(e^{-j(\beta L_0 + \phi)}) = 0$ holds approximately. (c) Illustration of the reflection of the normal magnetic field of the fundamental hybrid in the 3D model, r and θ are the reflection coefficient and phase shift respectively.

there is also a damped oscillation of the total decay rate with the length of the computation domain, and the tendency of achieving higher accuracy for γ_{total} when L_0 is lengthened, which is similar to the length dependence study of the total decay rate for the nanowire. Nevertheless, there are two distinctions between the two plots: I) The variation of the total decay rate for the square plasmonic waveguide is much larger than that for the metallic nanowire; II) The variation of the total decay rate for the square plasmonic waveguide with L_0 primarily stems from the reflection of two different modes, which are indicated by two different periods in the damped oscillation. The reflection of the fundamental mode, which is supposed to be absorbed at the boundaries, is responsible for the oscillation with the period of 200nm, the other oscillation with the period of 370 nm results from the reflection of a quasi guided mode, denoted by E_{qg} . The explanation is the following, the boundary condition defined by Eq. (11a) can completely absorb the matched pure TM mode, while it is not true for the boundary condition defined by Eq. (13) for the hybrid mode, and a significant reflection from a quasi guided mode also exists for the square plasmonic waveguide. For the hybrid mode the last term in Eq. (10) relies not only on the tangential components of the electric (magnetic) field, but also on the normal component of the electric (magnetic) field, which is intrinsically lost on the boundary in the vector element formulation of the 3D numerical model³². Our interpretation is that, even though the normal component of the electric field can be included on the boundaries by Eq. (13), the normal component of the magnetic field is essentially missing in the 3D numerical model with the square plasmonic waveguide, resulting in the reflections in our vector element formulation^{34,35}. However, in Fig. 6(a), it appears that the points for which $real(e^{-j(\beta L_0 + \phi)}) = 0$ holds approximately converge quickly with minimum impact of the reflection from the fundamental hybrid mode. The mode E_{qg} , with effective wavelength of 740.07 nm, is characterized by the material properties of the waveguide and is rather insensitive to the size of the metallic core. Compared with other quasi guided modes or radiation modes, the mode E_{qg} has a relatively significant contribution to the γ_{total} , the normalized spontaneous emission rate is 0.107. Since no extra effort is made to prevent the reflections from any components of the mode E_{qg} , it is understandable that the induced reflections give rise to several peaks in Fig. 6(a).

The normal component of the magnetic field of the fundamental mode in the 3D model can be obtained by a 2D eigenvalue calculation, $H_{n,l} = \sqrt{\frac{\gamma_{pl}P_0}{P_{2d}}} H_{2d}^n e^{-j(\beta l + \phi)}$, where l is the distance from the observation plane to the emitter. Similarly, the reflected normal component of the magnetic field at the position of the emitter can be obtained by taking into account the phase shift due to propagation and reflection, $H_{n,0}^r = r \sqrt{\frac{\gamma_{pl}P_0}{P_{2d}}} H_{2d}^n e^{-j(2\beta L_0 + \phi + \theta)}$, as shown in Fig. 6 (c). The reflected normal component of the magnetic field will “generate” a perturbation term E_x^r to the original E_x component, the real part of which is integrated to calculate the total power dissipation. According to Table I, the reflected term E_x^r from the fundamental hybrid mode is given by

$$E_x^r = -\frac{1}{\omega \varepsilon} (\nabla_t \times \bar{n} (r \sqrt{\frac{\gamma_{pl}P_0}{P_{2d}}} H_{2d,m}^z e^{-j(2\beta L_0 + \phi + \theta)}))_x. \quad (14)$$

The real part of E_x^r can be zero when L_0 is appropriately chosen, therefore, the obtained total decay rates are expected to approach the true value more closely due to the vanishing contribution of E_x^r to the total decay rate. In Fig. 6(a), at the points with marked ellipses, the half model length L_0 fits the requirement ($\text{real}(E_x^r) = 0$), and we also found that the phase shift θ is required approximately to be $\pi/2$. Further examining the phase shift θ involves technical details regarding the implementation of the vector element formulation of the finite element method, which is beyond the scope of the present paper, and we refer to the references^{32,34,35,36}. From Fig. 6(b), we estimate the relative error on the computed data for the square plasmonic waveguide to be $\pm 2\%$, when L_0 is larger than $1 \mu\text{m}$.

III. RESULT AND DISCUSSION

In this section, the numerical method is applied to the two cases, the metallic nanowire and the square plasmonic waveguide. For the metallic nanowire, we compared our numerical calculations with the quasistatic approximation, which was studied by Chang et al²⁴. As can be seen in Fig. 7, our numerical results agree well with the quasistatic approximation when the radius of the metallic nanowire is less than 20 nm, while it is 5-10 times larger when the radius is 100 nm. The deviation between the two methods increases when the radius becomes larger. The results of the comparison can be understood if one realizes that the quasistatic approximation is valid only when the radius is much smaller than the wavelength. For the large wires, which has also been pointed out by Chang et al.²⁴, the full electrodynamic solutions predict significantly larger values of γ_{pl}/γ_0 and the β factor. The quasistatic approximation assumes that the magnetic field vanishes, thus the obtained solution of the electric field simply behaves as a static field. It is the same for the plasmonic mode, the penetration length of which in the dielectric medium is considerable shorter than that obtained from the full electrodynamic solutions, and therefore the quasistatic calculation predicts a lower coupling efficiency. In summary, our numerical calculation is consistent with the quasistatic approximation for the nanowire radii approaching 0, and the values from finite element simulation are generally larger than those obtained from the quasistatic approximation when the radius is beyond 20 nm.

We also studied the coupling of the quantum emitter with the square plasmonic waveguide. As shown in the inset in Fig. 8, the quantum emitter is oriented along the X axis, and the distance dependence of the plasmonic decay rates and spontaneous emission β factors is calculated as function of emitter position along the X axis. With optimized side length of the waveguide and distance of the emitter to the edge of the waveguide, the β factor can reach 80%.

IV. CONCLUSION

In conclusion, we developed a self-consistent model to study the spontaneous emission of a quantum emitter at nanoscale proximity to a plasmonic waveguide using the finite element method. The dyadic Green function of the guided modes supported by the plasmonic waveguide can be constructed numerically from the eigenmode analysis, and subsequently the normalized decay rate into the plasmonic channel can be extracted. The 3D finite element model is also implemented to calculate the total decay rate, including the radiative decay rate, nonradiative decay rate, and the plasmonic decay rate. In the 3D model, it is assumed that only one guided plasmonic mode is dominantly excited, which is normally true when the size of the cross section of the plasmonic waveguide is below 100 nm. Under such condition, the spontaneous emission β factor is calculated. We compared our numerical approach with the quasistatic approximation for the gold nanowire. We observe agreement with the quasistatic approximation for radii below 20 nm, where the quasistatic approximation is valid. For larger radii the FE simulation predicts approximately 5 times larger values. This is reasonable since the numerical model takes into account wave propagation, whereas the quasistatic approximation calculates the static field. We also applied our numerical model to calculate the spontaneous emission

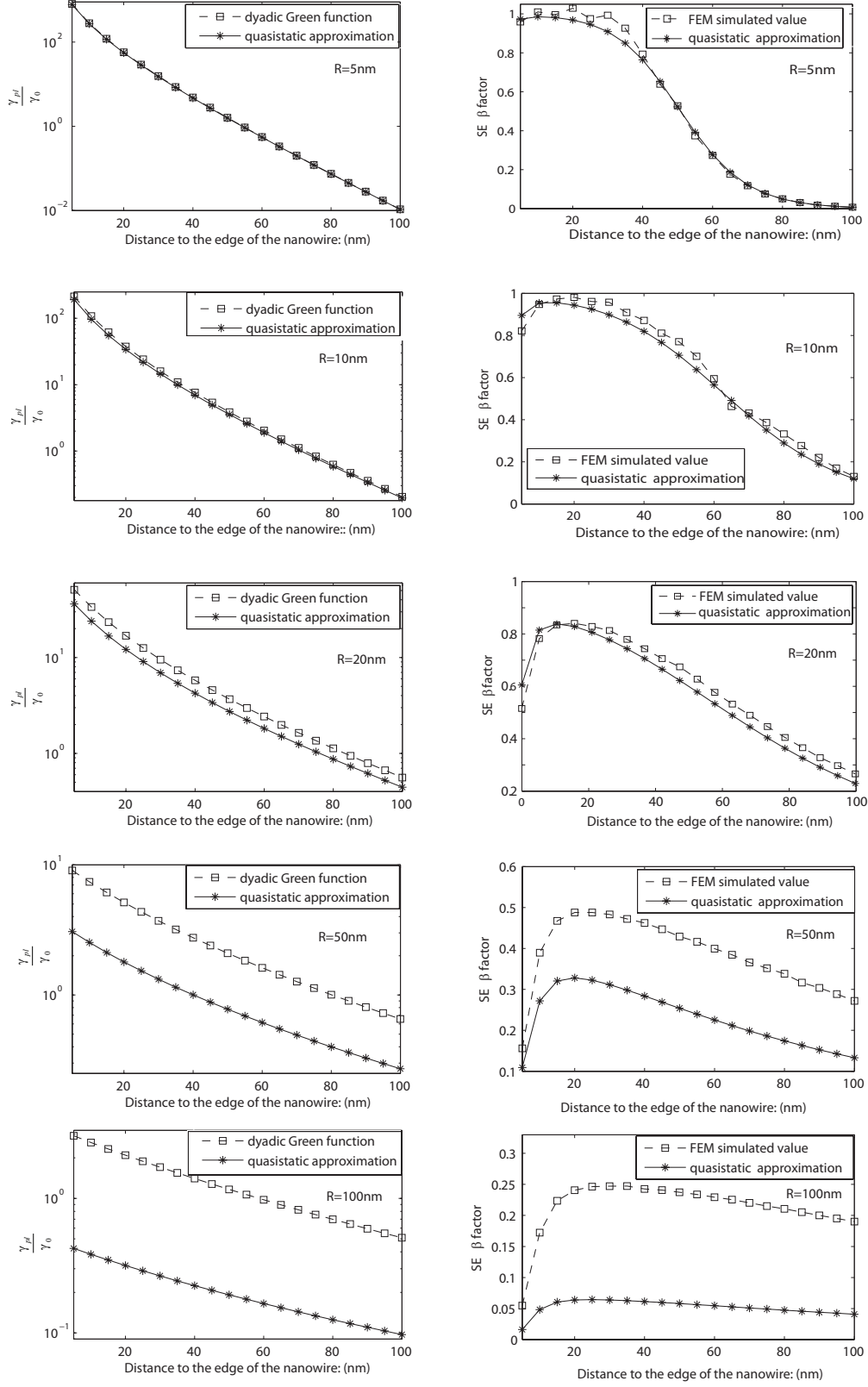


FIG. 7: Comparison of FEM simulated results based on the dyadic Green function with the quasistatic approximation for the metallic nanowire.

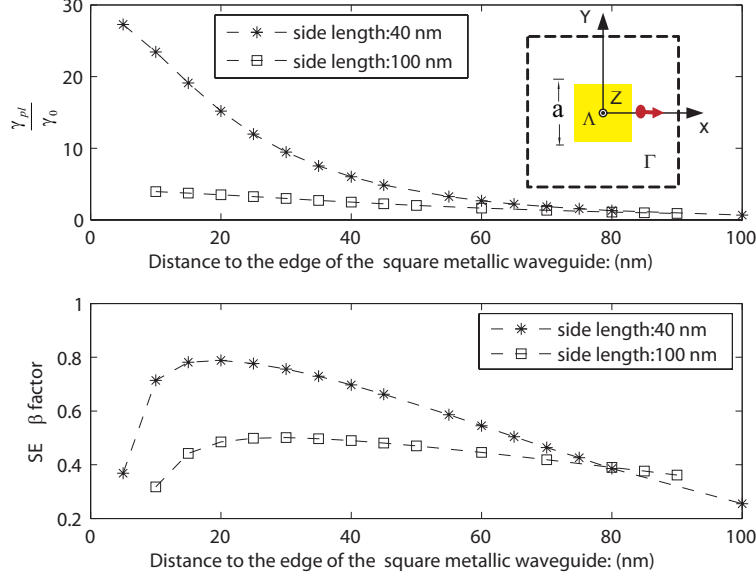


FIG. 8: Distance dependence of the plasmonic decay rates and spontaneous emission β factors for the square plasmonic waveguide.

of a quantum emitter coupled to a square plasmonic waveguide. The numerical calculations shows that spontaneous emission β factor up to 80% can be achieved for a horizontal dipole emitter, when the distance and the side length are optimized.

V. ACKNOWLEDGMENT

The authors would like to thank Anders S. Sørensen, Thomas Søndergaard, Andrei Lavrinenko and Darrick Chang for fruitful discussions. We gratefully acknowledge support from Villum Kann Rasmussen Fonden via the NATEC center.

-
- ¹ E. M. Purcell, Phys. Rev. **69**, 681 (1946).
 - ² H. P. Urbach and G. L. J. A. R. Rikken, Phys. Rev. A **57**, 3913 (1998).
 - ³ J. Johansen, S. Stobbe, I. S. Nikolaev, T. Lund-Hansen, P. T. Kristensen, J. M. Hvam, W. L. Vos, and P. Lodahl, Phys. Rev. B **77**, 073303 (2008).
 - ⁴ G. Björk, S. Machida, Y. Yamamoto, and K. Igeta, Phys. Rev. A **44**, 669 (1991).
 - ⁵ J. M. Gérard, B. Sermage, B. Gayral, B. Legrand, E. Costard, and V. Thierry-Mieg, Phys. Rev. Lett. **81**, 1110 (1998).
 - ⁶ E. Yablonovitch, Phys. Rev. Lett. **58**, 2059 (1987).
 - ⁷ P. Lodahl, A. F. van Driel, I. S. Nikolaev, A. Irman, K. Overgaard, D. Vanmaekelbergh, and W. L. Vos, Nature **430**, 654 (2004).
 - ⁸ D. Kleppner, Phys. Rev. Lett. **47**, 233 (1981).
 - ⁹ T. Lund-Hansen, S. Stobbe, B. Julsgaard, H. Thyrrestrup, T. Süner, M. Kamp, A. Forchel, and P. Lodahl, Phys. Rev. Lett. **101**, 113903 (2008).
 - ¹⁰ A. V. Akimov, A. Mukherjee, C. L. Yu, D. E. Chang, A. S. Zibrov, P. R. Hemmer, H. Park, and M. D. Lukin, Nature **450**, 402 (2007).
 - ¹¹ D. E. Chang, A. S. Sørensen, P. R. Hemmer, and M. D. Lukin, Phys. Rev. Lett. **97**, 053002 (2006).
 - ¹² K. Kneipp, Y. Wang, H. Kneipp, L. T. Perelman, I. Itzkan, R. R. Dasari, and M. S. Feld, Phys. Rev. Lett. **78**, 1667 (1997).
 - ¹³ S. Nie and S. R. Emory, Science **275**, 1102 (1997).
 - ¹⁴ N. E. Hecker, R. A. Hopfel, N. Sawaki, T. Maier, and G. Strasser, Appl. Phys. Lett. **75**, 1577 (1999).
 - ¹⁵ K. B. Crozier, A. Sundaramurthy, G. S. Kino, and C. F. Quate, J. Appl. Phys. **94**, 4632 (2003).
 - ¹⁶ T. H. Taminiau, F. D. Stefani, F. B. Segerink, and N. F. van Hulst, Nature Photonics **2**, 234 (2008).

- ¹⁷ S. Kühn, U. Hakanson, L. Rogobete, and V. Sandoghdar, Phys. Rev. Lett. **97**, 017402 (2006).
- ¹⁸ D. E. Chang, A. S. Sørensen, E. A. Demler, and M. D. Lukin, Nature Phys. **3**, 807 (2007), 0706.4335.
- ¹⁹ W. L. Barnes, A. Dereux, and T. W. Ebbesen, Nature **424**, 824 (2003).
- ²⁰ A. V. Zayats, J. Elliott, I. I. Smolyaninov, and C. C. Davis, Applied Physics Letters **86**, 151114 (2005).
- ²¹ I. I. Smolyaninov, J. Elliott, A. V. Zayats, and C. C. Davis, Phys. Rev. Lett. **94**, 057401 (2005).
- ²² J. Takahara, S. Yamagishi, H. Taki, A. Morimoto, and T. Kobayashi, Opt. Lett. **22**, 475 (1997).
- ²³ S. I. Bozhevolnyi, V. S. Volkov, E. Devaux, J.-Y. Laluet, and T. W. Ebbesen, Nature **440**, 508 (2006).
- ²⁴ D. E. Chang, A. S. Sørensen, P. R. Hemmer, and M. D. Lukin, Phys. Rev. B **76**, 035420 (2007).
- ²⁵ G. Veronis and S. Fan, Opt. Lett. **30**, 3359 (2005).
- ²⁶ Y. C. Jun, R. D. Kekapture, J. S. White, and M. L. Brongersma, Phys. Rev. B **78**, 153111 (2008).
- ²⁷ E. D. Palik, *Handbook of optical constants of solids II* (Academic Press, 1991).
- ²⁸ J. Jung, T. Søndergaard, and S. I. Bozhevolnyi, Phys. Rev. B **76**, 035434 (2007).
- ²⁹ T. Søndergaard and B. Tromborg, Phys. Rev. A **64**, 033812 (2001).
- ³⁰ L. Novotny and B. Hecht, *Principles of Nano Optics* (Cambridge University Press, 2006), 2nd ed.
- ³¹ A. W. Snyder and J. Love, *Optical Waveguide Theory* (Springer, 1983).
- ³² J. M. Jin, *The Finite Element Method in Electromagnetics* (Wiley-IEEE Press, 2002), 2nd ed.
- ³³ J. D. Jackson, *Classical Electrodynamics* (John Wiley & Sons, Inc., 1999), 3rd ed.
- ³⁴ V. N. Kanellopoulos and J. P. Webb, IEEE Trans. Microw. Theory Tech. **43**, 2168 (1995).
- ³⁵ J. P. Webb, IEEE Trans. Magnetics **29**, 1460 (1993).
- ³⁶ M. M. Botha and D. B. Davidson, IEEE Trans. Antennas Propag. **54**, 3499 (2006).
- ³⁷ <http://www.comsol.com>